Clays and Clay Minerals, Vol. 69, No. 2:243–253, 2021

MULTIPLE HIERARCHICAL HETEROJUNCTION g-C_3N_4/LDH/Ag_3PO_4 WITH ENHANCED VISIBLE-LIGHT PHOTOCATALYTIC ACTIVITY FOR Cr(VI) REDUCTION

Chao-Rong Chen[1], Hong-Yan Zeng[1,*], Jie Xiong[1], De-Shun An[1], and Song Li[1]
[1] College of Chemical Engineering, Xiangtan University, Xiangtan 411105, Hunan, China

Abstract—Semiconductor photocatalysis has been regarded as one of the most promising methods for treatment of Cr(VI)-containing wastewater, but the high recombination rate of photogenerated carriers and photocorrosion have limited severely its practical application. The objective of the current study was to employ a layered double hydroxide (LDH) to mitigate these problems by designing and constructing a multiple heterojunction system of g-C_3N_4/LDH/Ag_3PO_4 (CNLDHAP) through a two-step hydrothermal route. The structures, morphologies, chemical states, and optical properties of the products were investigated systematically. The CNLDHAP composite showed superior photocatalytic activity for Cr(VI) reduction than that of the individual components under visible-light irradiation. The composite exhibited high photocatalytic reduction stability after five recycles. The enhanced photocatalytic performance may originate from the very efficient separation of photogenerated carriers of the multiple heterojunction system. Possible photocatalytic mechanisms for the reduction of Cr(VI) over the CNLDHAP composite photocatalyst are proposed.

Keywords—Ag_3PO_4 · Cr(VI) reduction · LDH · Multiple heterojunction · Photocatalytic

INTRODUCTION

Heavy-metal pollution of surface and underground water sources has threatened ecological environments and human health (Chen et al. 2018; Luo et al. 2015, 2019; Wang et al. 2019). As a typical, toxic, heavy-metal ion, hexavalent chromium (Cr(VI)), derived mainly from chromate-related industrial processes such as wood treatment, leather tanning, and textile industries, has received significant attention in the literature (Nanda et al. 2017; Velegraki et al. 2018; Yuan et al. 2019). Semiconductor-mediated photocatalytic reduction is considered to be a clean way to remove toxic Cr(VI) from wastewater (Jing et al. 2017; Zhong et al. 2016). As a silver-based photocatalyst, Ag_3PO_4 has aroused great attention due to the large quantum yield and the visible-light response (Chen et al. 2019a; Shao et al. 2019). Some problems remain, however, during the photocatalytic process: (1) the high recombination rate of the photogenerated electron holes (Zhou et al. 2017); (2) the serious photocorrosion phenomenon ($Ag_3PO_4 \rightarrow Ag^0$) (Xu et al. 2014); and (3) the relatively large particle size of Ag_3PO_4 (Abroshan et al. 2018). Many studies involving the combination of Ag_3PO_4 with other semiconductor materials to construct heterojunction composites have attempted to solve these problems (Dhanabal et al. 2018; Kumar et al. 2013; Liu et al. 2019a; Tian et al. 2019; Wan et al. 2017). Although the photocatalytic activity of these hybrid composites has been improved to some degree above that of pure Ag_3PO_4, a more stable and more efficient Ag_3PO_4-based photocatalyst is still needed.

Layered double hydroxides (LDHs), consisting of positively charged brucite-like layers and negatively charged interlayer anions, have attracted much attention in photocatalysis and photoelectrocatalysis (Wu et al. 2018; Zhao et al. 2015, 2016). In previous work, ZnAl LDH was shown to be an effective catalyst support for the photocatalyst due to its 2D layered structure, large surface area, and abundant hydroxyl groups (Chen et al. 2019b). The net trap confinement effects of LDH can inhibit effectively the aggregation of particles. Because of its band gap of 2.1 eV, CoAl LDH is considered to offer promise as a photocatalyst; it is also low-cost, environmentally friendly, and has appropriate oxidation–reduction potential (Kumar et al. 2017; Li et al. 2017; Wang et al. 2018). The relatively poor electrical conductivity and high electrical resistance of CoAl LDH restrict severely its photocatalytic application, however (Fang et al. 2012; Peng et al. 2017a).

To solve these problems, some studies focused on incorporation in CoAl LDH of conductive carbon materials, e.g. carbon nanotubes (Zhang et al. 2016a), graphitic carbon nitride (Jo and Tonda 2019), and fluorinated graphene (Peng et al. 2017a), which resulted in significant improvement in the electrical conductivity and electrical resistance. The introduction of conductive carbon material might, therefore, be an effective strategy for enhancing the photocatalytic performances of heterojunction photocatalysts. As a metal-free conjugated polymer semiconductor, graphitic carbon nitride (g-C_3N_4) has become a focus of attention due to its appropriate electronic band structure, low cost, and easy preparation (Li et al. 2019; Zheng et al. 2015).

* E-mail address of corresponding author: hyzeng@xtu.edu.cn
DOI: 10.1007/s42860-021-00121-0

Moreover, g-C_3N_4 with its unique delocalized π-conjugated structure and good conductivity can provide a larger interface contact area and promote photogenerated charge separation (Jo and Tonda 2019; Shakeel et al. 2019).

Based on the discussion above, the objectives of the present study were to design a multiple heterojunction system of g-C_3N_4/LDH/Ag_3PO_4 (CNLDHAP) composite which could be constructed via a two-step hydrothermal pathway, to evaluate its photocatalytic activity toward Cr(VI) reduction under visible light irradiation, and to confirm the stability and reusability of the CNLDHAP composite upon reuse or recycling. A final objective was to propose a probable mechanism by which the photocatalysis occurs.

EXPERIMENTS

Materials

$Co(NO_3)_2{\cdot}6H_2O$, $Al(NO_3)_3{\cdot}9H_2O$, Na_2HPO_4, $AgNO_3$, NaOH, HCl, and urea were purchased from Sinopharm Chemical Reagent Co., Ltd. China; $K_2Cr_2O_7$ was purchased from Shanghai Macklin Biochemical Technology Co., Ltd. China. All the chemical reagents were of analytical grade and used without further purification.

Synthesis of g-C_3N_4

Pure g-C_3N_4 was prepared by the thermal polymerization of urea. 15 g of urea was placed in a crucible with a cover, and heated at 550°C for 3 h with a heating rate of 5°C min^{-1}. After cooling naturally to room temperature, the yellow product was ground to powder and the g-C_3N_4 obtained.

Synthesis of g-C_3N_4/LDH/Ag_3PO_4 Composites

The preparation process of g-C_3N_4/LDH/Ag_3PO_4 composite was as illustrated in Fig. 1. Briefly, g-C_3N_4 (80 mg) was mixed in 80 mL of deionized water and treated ultrasonically for 60 min. $Co(NO_3)_2{\cdot}6H_2O$ (1.833 g), $Al(NO_3)_3{\cdot}9H_2O$ (0.788 g), and urea (3.405 g) were added to the solutions above and stirred for 120 min, and then heated at 110°C for 24 h. The sample obtained was denoted as g-C_3N_4/LDH. Subsequently, 0.8 g of g-C_3N_4/LDH was dispersed in 50 mL of deionized water and an appropriate amount of $AgNO_3$ (0.380, 0.630, 0.882, or 1.13 g) was dissolved in the above suspensions and stirred for 120 min. After that, 20 mL of a certain concentration of Na_2HPO_4 (0.037, 0.062, 0.087, or 0.111 M) was added dropwise to the mixture solution and stirred for 12 h at room temperature. Finally, the resulting suspension was centrifuged at 4192.5×*g* and washed thoroughly with deionized water, and dried in vacuum at 60°C overnight. According to the calculated weight percent of Ag^+ in the g-C_3N_4/LDH, a series of g-C_3N_4/LDH/Ag_3PO_4 composites with various weight percentages of Ag^+ were denoted as CNLDHAP30, CNLDHAP50, CNLDHAP70, and CNLDHAP90, respectively. For comparison, the Ag_3PO_4 and LDH were also synthesized following a similar procedure.

Characterization

Powder X-ray diffraction (XRD) measurements were performed using a Rigaku D/max 2550PC (Tokyo, Japan) instrument with CuKα irradiation (λ = 1.5405 Å). The scan step was 0.02°2θ with a filament current of 30 mA and a voltage of 40 kV. Scanning electron microscopy (JEOL JSM-6700F, Tokyo, Japan) and transmission electron microscopy (FEI Talos F200S, Waltham, Massachusetts, USA) were used to examine the morphologies and microstructures of the samples. X-ray photoelectron spectroscopy (XPS) analyses were carried out using a Thermo Fisher Scientific K-Alpha spectrometer (Waltham, Massachusetts, USA). The C 1s peak from the adventitious carbon-based contaminant with a binding energy of 284.8 eV was used as the reference for calibration. UV-Visible diffuse reflectance spectra (UV-Vis DRS) were measured by using a UV-Visible spectrophotometer (Shimadzu UV-2550, Tokyo, Japan). Photoluminescence (PL) spectra were recorded using a fluorescence spectrophotometer (F-4600, Tokyo, Japan) at room temperature. The scanning speed was 1200 nm/min and the width of the emission slit was 5.0 nm. Mott-Schottky plots were created using an electrochemical workstation (CHI660E, Shanghai Chenhua Instrument Co. Ltd., China) and the standard three-electrode system was immersed in 0.5 mol L^{-1} Na_2SO_4 solution at room temperature. Dur-

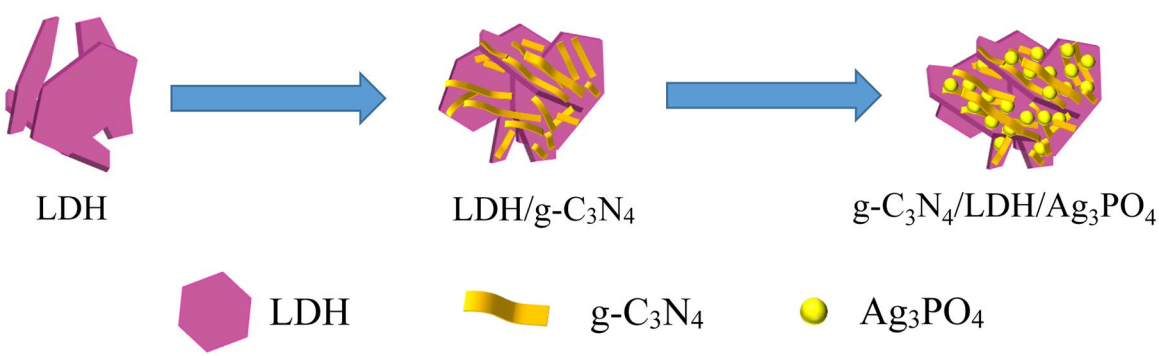

Fig. 1 Schematic diagram illustrating the fabrication process for the g-C_3N_4/LDH/Ag_3PO_4 composite

https://doi.org/10.1007/s42860-021-00121-0 Published online by Cambridge University Press

ing the measurements, a saturated calomel electrode (SCE) served as the reference electrode and Pt foil as the counter electrode. The working electrodes were prepared by coating the indium-doped tin oxide (ITO) conductive glass with g-C_3N_4, Ag_3PO_4, and LDH ethanol solution.

Photocatalytic Experiments

Photocatalytic activities of the as-synthesized photocatalysts were evaluated by examining the photoreduction efficiency of Cr(VI). A 300 W Xe lamp equipped with a 420 nm cut-off filter was used as the visible light source. In the photocatalytic experiments, 100 mg of photocatalyst was dispersed in 100 mL of 50 mg·L^{-1} Cr(VI) aqueous solution. Prior to irradiation, the mixed solution was stirred vigorously in the dark for 30 min to establish an adsorption–desorption equilibrium between the photocatalyst and Cr(VI). At regular time intervals (15 min), 2 mL of the reaction solution was collected and centrifuged at 16,770×*g*. Subsequently, the Cr(VI) content was determined by the 1,5-diphenylcarbazide method using a UV-Vis spectrophotometer (752 N spectrophotometer, Shanghai Spectrum Instruments Co., Ltd., China) at 540 nm (Chen et al. 2018).

RESULTS AND DISCUSSION

Structural Characterization

The phase structures of the g-C_3N_4, Ag_3PO_4, LDH, g-C_3N_4/LDH, CNLDHAP30, CNLDHAP50, CNLDHAP70, and CNLDHAP90 composites were investigated by XRD (Fig. 2a). The g-C_3N_4 exhibited diffraction peaks at ~13.1 and 27.3°2θ corresponding to the (100) and (002) planes of g-C_3N_4 (Sun et al. 2019). For the Ag_3PO_4, the diffraction peaks located at 20.9, 29.7, 33.3, 36.6, 47.8, 52.7, 55.2, 57.2, 61.6, and 71.8°2θ were attributed to the (110), (200), (210), (211), (310), (222), (320), (321), (400), and (421) planes of the body-centered cubic structure of Ag_3PO_4 (Chen et al. 2019a). As for LDH, the main peaks at 11.5, 23.2, 34.1, 38.5, 60.1, and 61.2°2θ were well indexed to the (003), (006), (012), (015), (110), and (113) planes of CoAl layered double hydroxides (Jo and Tonda 2019). For the CNLDHAP composites, all of the characteristic peaks of LDH and Ag_3PO_4 were observed clearly, indicating that the formation of a ternary composite had no effect on their crystalline structure. No obvious characteristic diffraction peaks of g-C_3N_4 were detected, so it is either absent or less than the XRD detection limit.

The FTIR spectra were collected to identify bonding information in the samples (Fig. 2b). The peak at ~3200 cm^{-1} was ascribed to a N – H stretching vibration from the uncondensed amino groups on g-C_3N_4 (Tonda et al. 2018). The peaks in the region 1100 to 1650 cm^{-1} were assigned to the typical stretching vibration of C – N and C = N heterocycles, and the peak at ~810 cm^{-1} arose from the triazine rings of g-C_3N_4 (Wang et al. 2014). The broad absorption band at ~3450 cm^{-1} was assigned to the stretching vibrations of surface hydroxyl groups on LDH (Chen et al. 2017), while the peaks at ~1360 and ~1637 cm^{-1} were attributed to the bending vibration of CO_3^{2-} and interlayer water molecules of LDH, respectively (Peng et al. 2017a; Yang et al. 2019). The peaks below ~800 cm^{-1} were ascribed to the stretching and bending vibration of a metal–oxygen bond (Co – O and Al – O) (Peng et al. 2017b). As for the CNLDHAP composites, the peaks at ~558 and ~1010 cm^{-1} were assigned to the asymmetric stretching vibration of P – O in PO_4^{3-}.

The morphological features of g-C_3N_4, Ag_3PO_4, LDH, g-C_3N_4/LDH, and CNLDHAP70 were examined by SEM. The Ag_3PO_4 exhibited a regular spherical shape with smooth surface, while the g-C_3N_4 displayed an irregular shape with a corrugated structure (Fig. 3a, b). The LDH (Fig. 3c) showed a thin hexagonal shape with an average lateral size between ~1.5 and 2.0 μm, which conformed to the typical structural characteristic of hydrotalcites. The g-C_3N_4/LDH (Fig. 3d) showed an open hierarchical structure with the thin hexagonal LDH sheets embedded randomly in the wrinkled g-C_3N_4. The CNLDHAP70 composite maintained the morphological feature of g-C_3N_4/LDH and the Ag_3PO_4 nanoparticles were kept in a well-dispersed state in the composites (Fig. 3e). In addition, the CNLDHAP70 composite was also characterized by TEM (Fig. 3f) and the results revealed that the g-C_3N_4 crystals overlapped and adhered tightly to the surface of LDH. The close contact among g-C_3N_4, LDH, and Ag_3PO_4 indicated a well-formed heterostructure interface between them, which could benefit the separation and transfer of the photogenerated carriers.

The chemical composition and chemical states of the CNLDHAP70 composite were analyzed by XPS (Fig. 4). The C 1s spectrum could be divided into four different peaks at 284.4, 286.5, 288.2, and 285.5 eV (Fig. 4a), which were ascribed to the C = C, C = O, N = C–N, and C–O bonds, respectively (Shakeel et al. 2019; Zhang et al. 2016b). The two peaks of Ag $3d_{5/2}$ and Ag $3d_{3/2}$ at 368.4 and 374.4 eV in the Ag 3d spectrum were attributed to Ag^+ ions in Ag_3PO_4 (Fig. 4b), indicating that the silver existed in the form of Ag^+ in the CNLDHAP70 (Chen et al. 2019a). Meanwhile, the peak at 132.8 eV in the P 2p spectrum (Fig. 4c) corresponded to P^{5+} ions in Ag_3PO_4 (Tan et al. 2017). For the O 1s spectrum (Fig. 4d), the peaks at 530.4, 531.6, and 532.6 eV were ascribed to the lattice oxygen (O^{2-}), surface –OH groups, and surface-adsorbed water, respectively (Fettkenhauer et al. 2015). The Co 2p spectrum was separated into four peaks according to the Gaussian fitting method (Fig. 4e). The peaks of 780.5 and 796.7 eV were assigned to Co $2p_{3/2}$ and Co $2p_{1/2}$; the other two peaks at 785.5 and 802.1 eV belonged to the satellite peaks of Co(II), which demonstrated a high-spin Co^{2+} state in CNLDHAP70 (Ma et al. 2010). The peak at 73.8 eV in the Al 2p spectrum (Fig. 4f) corresponded well with the Al^{3+} in the brucite-like layers of LDH (Das et al. 2019).

The optical absorption properties of Ag_3PO_4, g-C_3N_4, LDH, g-C_3N_4/LDH, and CNLDHAP compo sites were

https://doi.org/10.1007/s42860-021-00121-0 Published online by Cambridge University Press

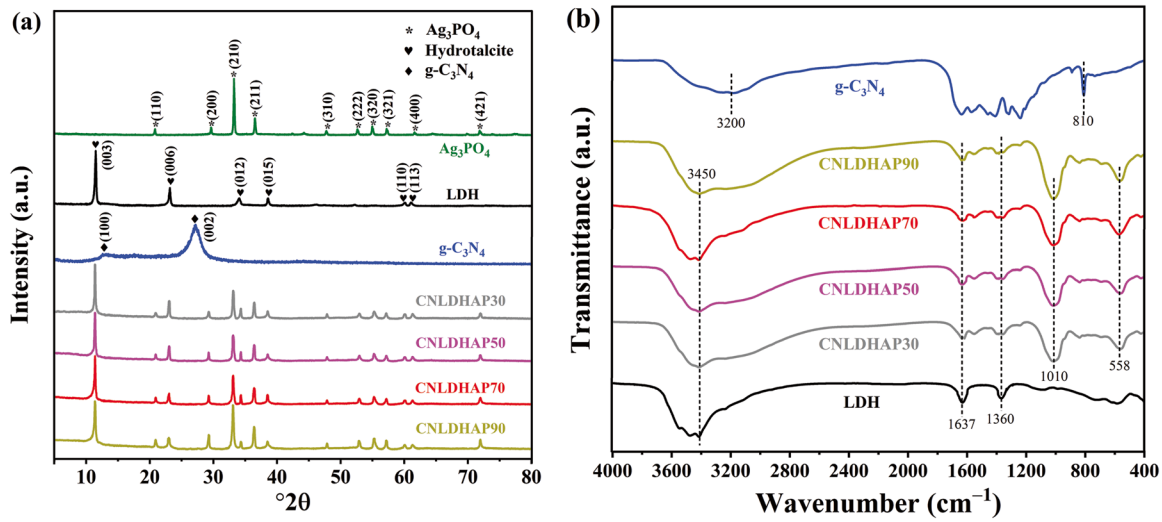

Fig. 2 **a** XRD patterns of the Ag_3PO_4, g-C_3N_4, LDH, and CNLDHAP composites, **b** FTIR spectra of the g-C_3N_4, LDH, and CNLDHAP composites

studied by UV-Vis DRS. The Ag_3PO_4 and g-C_3N_4 displayed a broad absorption in the visible region with absorption edges at ~530 and 460 nm, respectively (Fig. 5a). The LDH showed two distinct absorption bands in the whole spectrum: the strong absorption band below 300 nm resulted from ligand-to-metal charge transfer, and the absorption band at ~500 nm corresponded to d–d transitions of octahedral Co^{2+} within the brucite-like layers of CoAl-layered double hydrotalcites (Wang et al. 2018). Compared with the LDH, the g-C_3N_4/LDH exhibited an improved light absorption in the region between 200 and 450 nm. In particular, the absorption edges of all the CNLDHAP ternary composites demonstrated a remarkable red-shift compared to LDH, and the absorption intensity increased with the amount of Ag_3PO_4. The results suggested that CNLDHAP ternary composites could be promising as a visible light active photocatalyst. In addition, the band-gap energy (E_g) was obtained according to the Kubelka–Munk formula (Wang et al. 2018) (Fig. 5b). The E_g of g-C_3N_4, LDH, and Ag_3PO_4 were 2.65, 2.10, and 2.43 eV, respectively.

The charge separation efficiency of the products were studied using PL spectra (Fig. 6). The LDH showed two obvious emission peaks centered at ~400 and 448 nm, while the g-C_3N_4/LDH showed a weaker PL intensity, indicating a more efficient charge transfer and separation in the g-C_3N_4/LDH. Furthermore, the peak intensity of the CNLDHAP composites decreased further compared with both the LDH and g-C_3N_4/LDH. In particular, the PL intensity of the ternary composite decreased at first and then increased with increasing amount of Ag_3PO_4; the CNLDHAP70 showed the lowest PL intensity. This indicated that the moderate Ag_3PO_4 loading was favorable for charge separation efficiency, but the excessive dosage could become the recombination centers for the photogenerated charge carriers and be unfavorable for the reduction of Cr(VI).

Photocatalytic Behaviors on Cr(VI) Reduction

The photocatalytic activity of composite samples was evaluated by reducing Cr(VI) at pH 3 under visible light irradiation. A negligible change of Cr(VI) concentration in the absence of photocatalyst indicated that Cr(VI) aqueous solution was stable under visible light irradiation (Fig. 7a). The Ag_3PO_4, g-C_3N_4, and LDH possessed poor photocatalytic activities, and their reduction ratios for Cr(VI) were only 18.1, 23.0, and 33.5% after 120 min of irradiation. Furthermore, the Cr(VI) removal ratio of g-C_3N_4/LDH reached 56.9%, which indicated that coupling g-C_3N_4 and LDH was an effective way to improve the photocatalytic reduction activity for Cr(VI). Compared with g-C_3N_4/LDH, all of the CNLDHAP composites showed much greater photocatalytic-reduction efficiency. In particular, CNLDHAP70 exhibited the greatest photocatalytic activity, and 96.0% of Cr(VI) was reduced within 120 min of visible-light irradiation.

The pseudo-first order model ($-\ln(C/C_0) = kt$) was employed to investigate the photocatalytic reduction process (Liu et al. 2017). The results revealed that CNLDHAP70 had the largest value of k of 0.0235 min^{-1} (Fig. 7b), which was almost 15.67 and 11.75 times greater than that of g-C_3N_4 (0.0015 min^{-1}) and LDH (0.0020 min^{-1}), respectively. The CNLDHAP70 was selected for the recycling experiments and the results

https://doi.org/10.1007/s42860-021-00121-0 Published online by Cambridge University Press

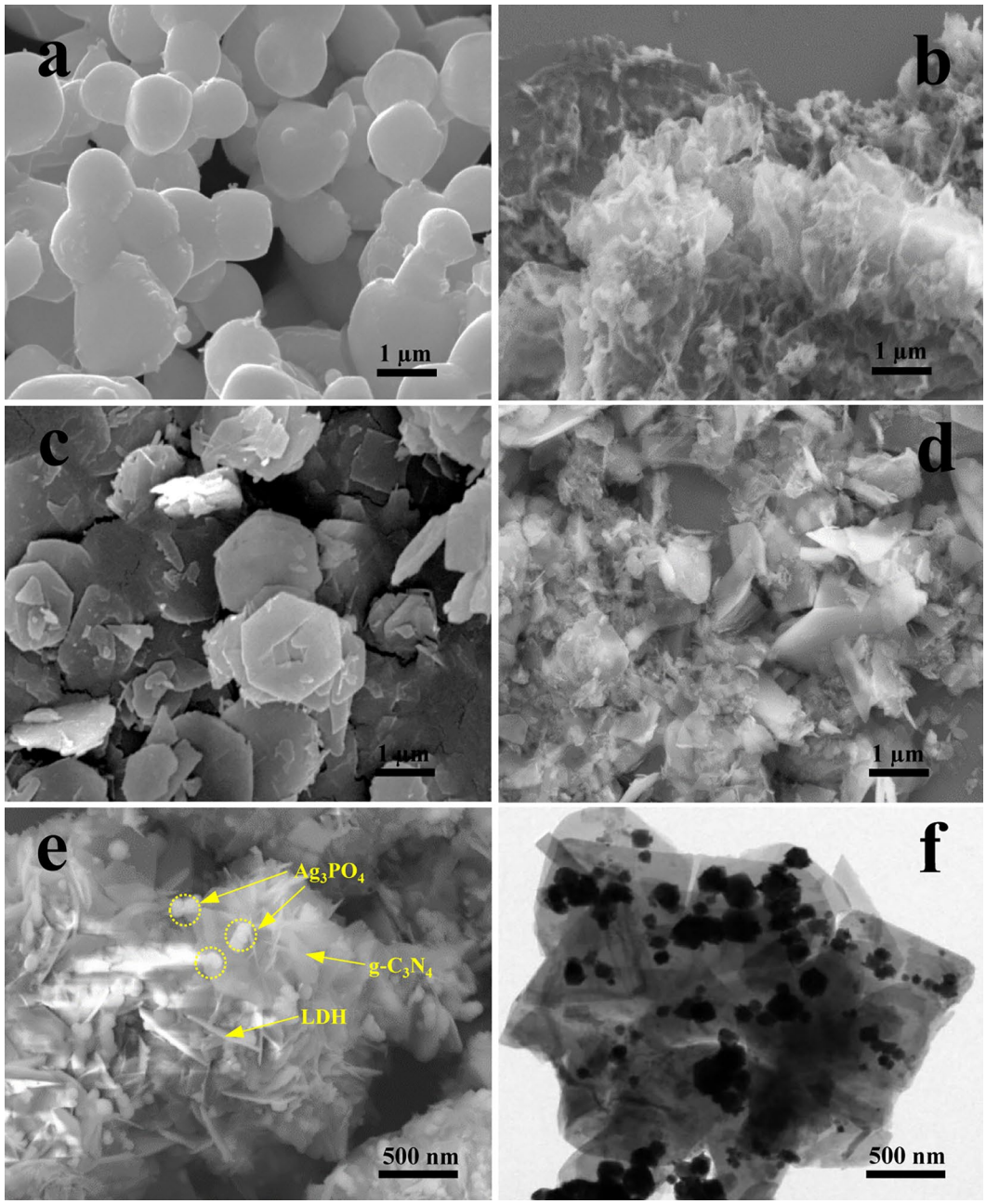

Fig. 3 SEM images of **a** Ag_3PO_4, **b** g-C_3N_4, **c** LDH, **d** g-C_3N_4/LDH, and **e** CNLDHAP70; **f** TEM image of CNLDHAP70

showed that CNLDHAP70 maintained a significant Cr(VI) reduction activity (86.0%) after five repeats of the experiment. The slight declines in Cr(VI) reduction efficiency were attributed to the active site coverage and to photocatalyst loss during the recycling process. The XRD patterns of CNLDHAP70 before and after Cr(VI) reduction were collected and the results revealed that the chemical structure of CNLDHAP70 composite was stable during the photocatalytic process (Fig. 7d). The chemical states of CNLDHAP70 after reaction were also investigated by XPS (Fig. 8a). The peaks at 576.9 and 586.9 eV contributed to the typical binding-energy

https://doi.org/10.1007/s42860-021-00121-0 Published online by Cambridge University Press

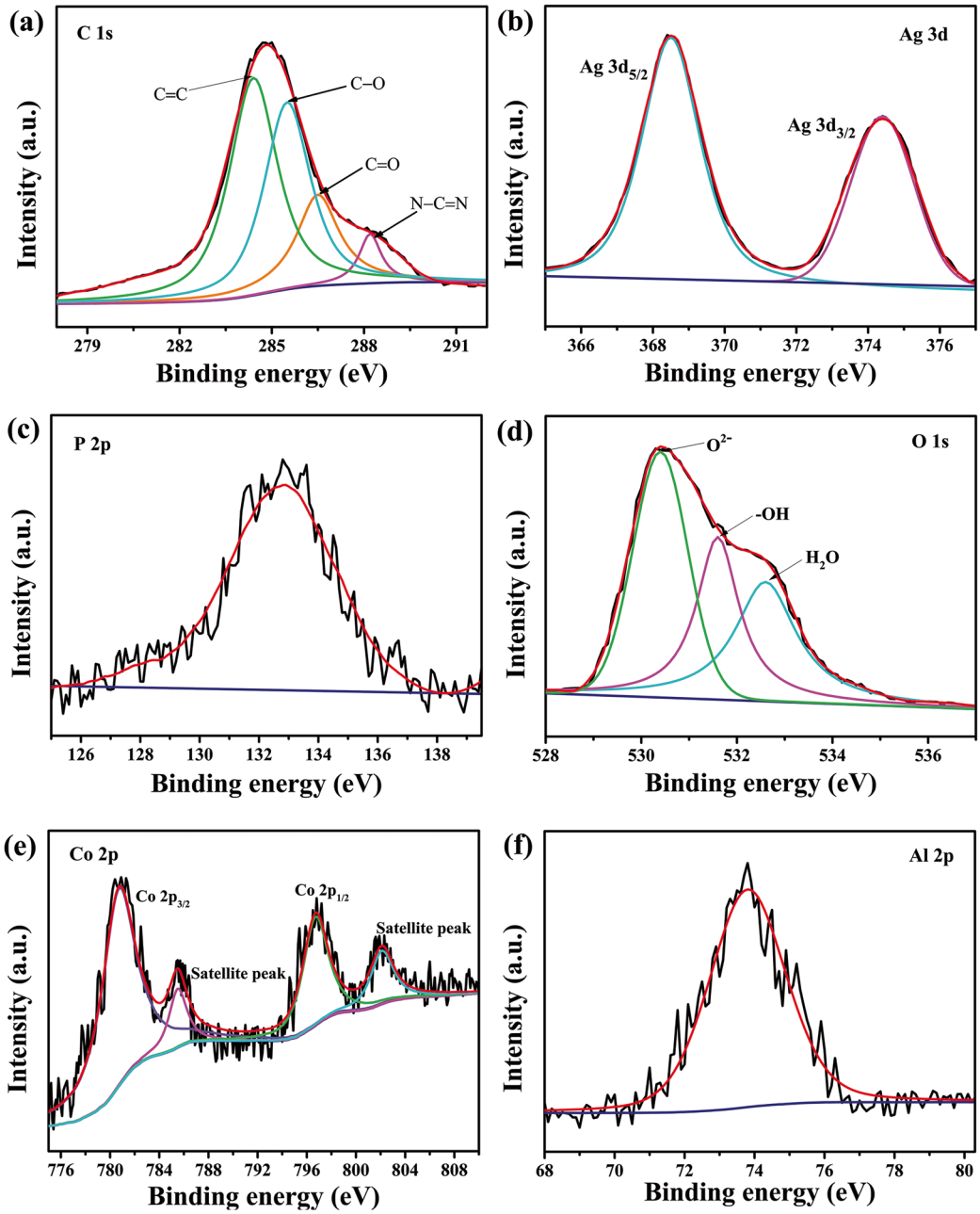

Fig. 4 XPS spectra of the CNLDHAP70 composite: **a** C 1s, **b** Ag 3d, **c** P 3p, **d** O 1s, **e** Co 2p, and **f** Al 2p

peaks of Cr(III) (Wu et al. 2015), which verified the successful reduction of Cr(VI). Meanwhile, the weak peak at the binding energy of 581.8 eV was due to the Cr(VI) on the surface of CNLDHAP70 adsorbed by electrostatic interaction.

Possible Mechanism for Cr(VI) Photocatalytic Reduction

In order to investigate the possible photocatalytic mechanism of Cr(VI) reduction, the band-edge positions were determined by the Mott-Schottky method. Both g-C_3N_4 and Ag_3PO_4 presented positive slopes in the linear region

https://doi.org/10.1007/s42860-021-00121-0 Published online by Cambridge University Press

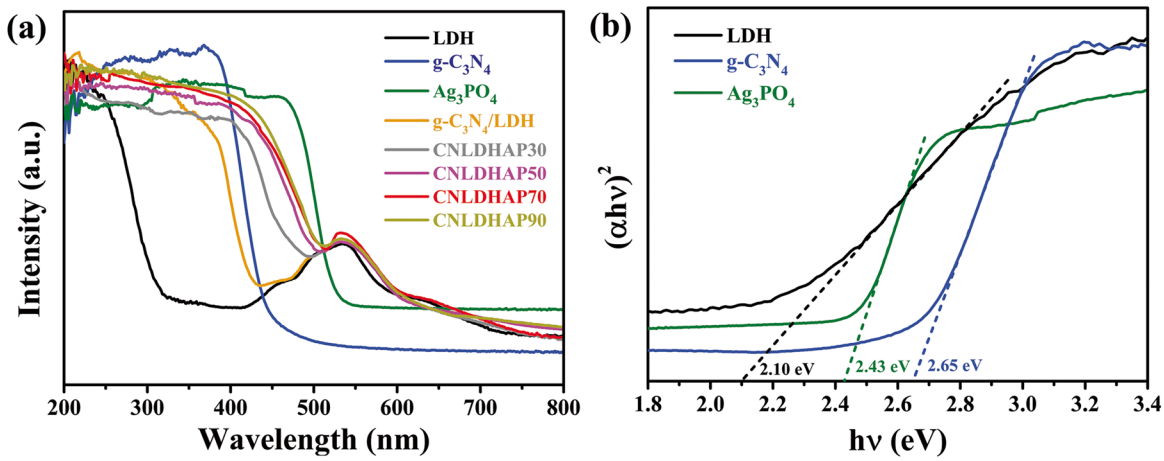

Fig. 5 **a** UV-vis DRS spectra of the Ag_3PO_4, g-C_3N_4, g-C_3N_4/LDH, and CNLDHAP composites; **b** Tauc plots of the Ag_3PO_4, g-C_3N_4, and LDH

(Fig. 8b, c), suggesting an n-type semiconductor nature (Kang et al. 2013). Generally, the flat band potential (E_{fb}) of n-type semiconductors is approximately equal to the conduction band (CB) potential (Xu et al. 2017). Thus, the CB positions of g-C_3N_4 and Ag_3PO_4 were –1.17 and 0.20 V vs. SCE (equivalent to −0.93 and 0.44 V vs. NHE), respectively. The LDH showed a negative slope in the Mott-Schottky plot (Fig. 8d), indicating p-type semiconductor behavior. Due to the E_{fb} of the p-type semiconductor being close to the valence band (VB) (Liu et al. 2019b), the VB of LDH was 1.16 V vs. SCE (equivalent to 1.40 V vs. NHE). According to the equation $E_{CB} = E_{VB} - E_g$ (Hu et al. 2019), the VB values of g-C_3N_4 and Ag_3PO_4 were 1.72 and 2.87 eV, and the CB of LDH was –0.70 eV.

Based on the results above, a potential multiple heterojunction mechanism was proposed to explain the enhanced photocatalytic activity of CNLDHAP composite photocatalyst. As shown in Fig. 9, the separation processes of photogenerated electron-hole pairs could be deduced to follow two possible paths. Under visible-light irradiation, g-C_3N_4, LDH, and Ag_3PO_4 were excited simultaneously to generate electron-hole pairs. With respect to charge-transfer Pathway I of the CNLDHAP composite, the electrons in the CB of g-C_3N_4 would migrate to the CB of LDH due to the potential difference between them. The holes in the VB of g-C_3N_4 would transfer first to the VB of LDH and then be eliminated by the electrons from the CB of Ag_3PO_4. Finally, the accumulated electrons in LDH could reduce Cr(VI) to Cr(III). The electron-transfer process of the CNLDHAP composite may also follow Pathway II, which is illustrated by the electrons in the CB of Ag_3PO_4 recombining with the holes in the VB of g-C_3N_4 and LDH, respectively, leaving the electrons in the CB of g-C_3N_4 and LDH to participate in the photocatalytic Cr(VI)-reduction reaction. Consequently, the synergy among those three semiconductors was effective in accelerating the spatial separation of photogenerated charge carriers and thus resulted in excellent photocatalytic performance of the ternary CNLDHAP composite photocatalyst.

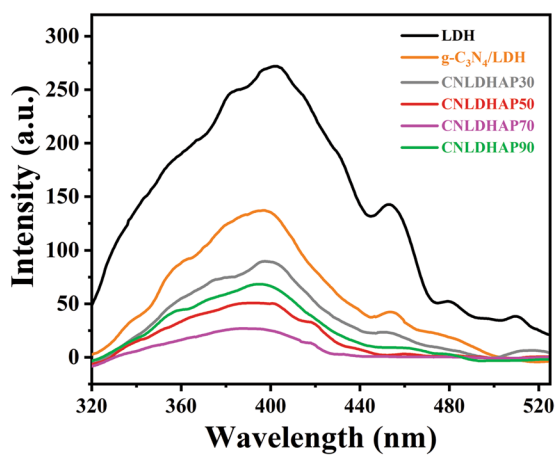

Fig. 6 PL spectra of the LDH, g-C_3N_4, g-C_3N_4/LDH, and CNLDHAP composites

https://doi.org/10.1007/s42860-021-00121-0 Published online by Cambridge University Press

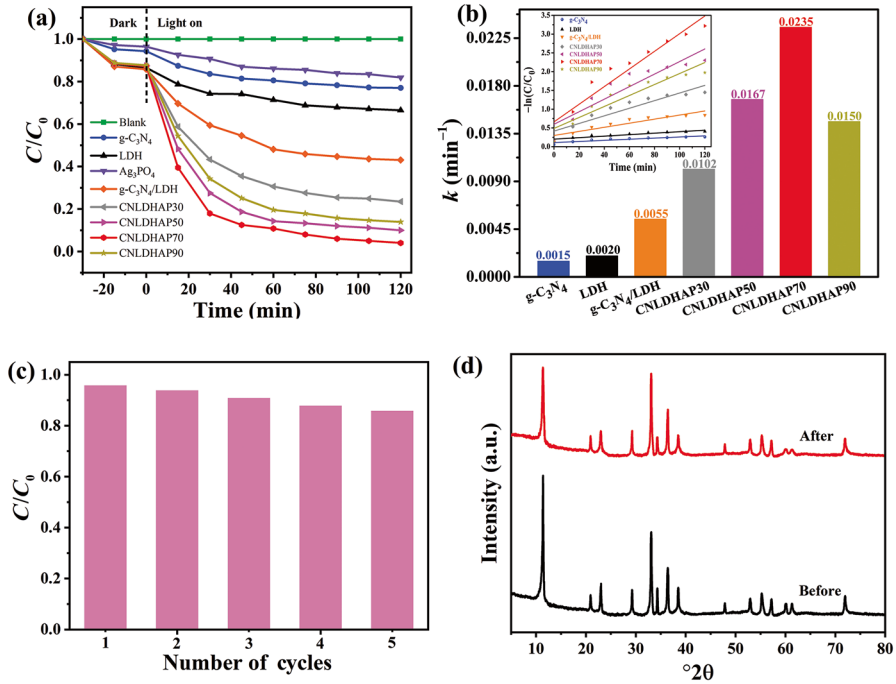

Fig. 7 **a** Photocatalytic reduction efficiency, **b** apparent reaction rate constants, pseudo-first order kinetics (inset in b), **c** reusability for Cr(VI) reduction under visible light irradiation, **d** XRD patterns of the CNLDHAP70 before and after photocatalytic reaction

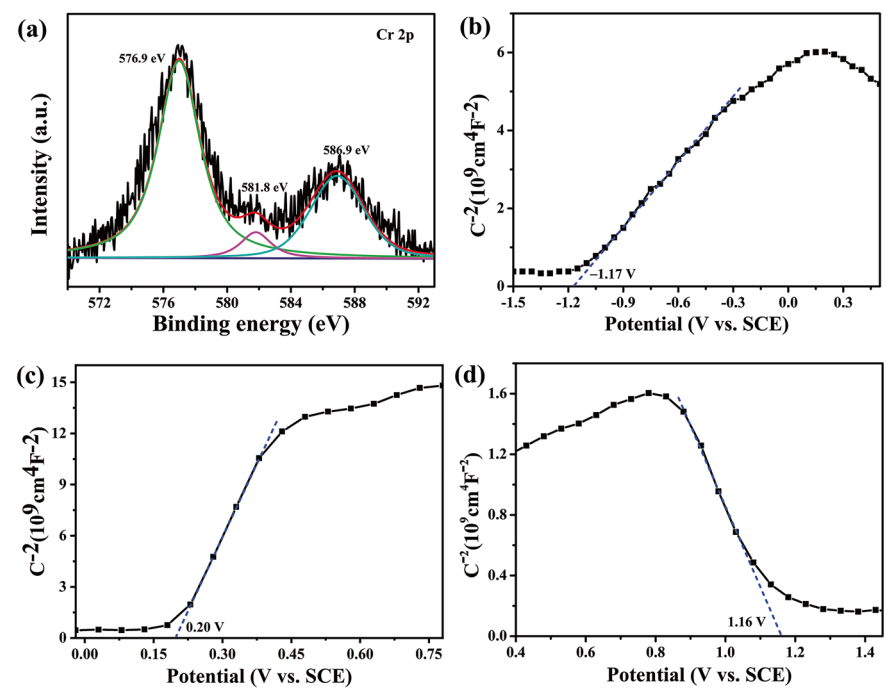

Fig. 8 **a** Cr 2p spectrum of the CNLDHAP70 composite after Cr(VI) reaction, Mott-Schottky plots of **b** g-C_3N_4, **c** Ag_3PO_4, and **d** LDH

https://doi.org/10.1007/s42860-021-00121-0 Published online by Cambridge University Press

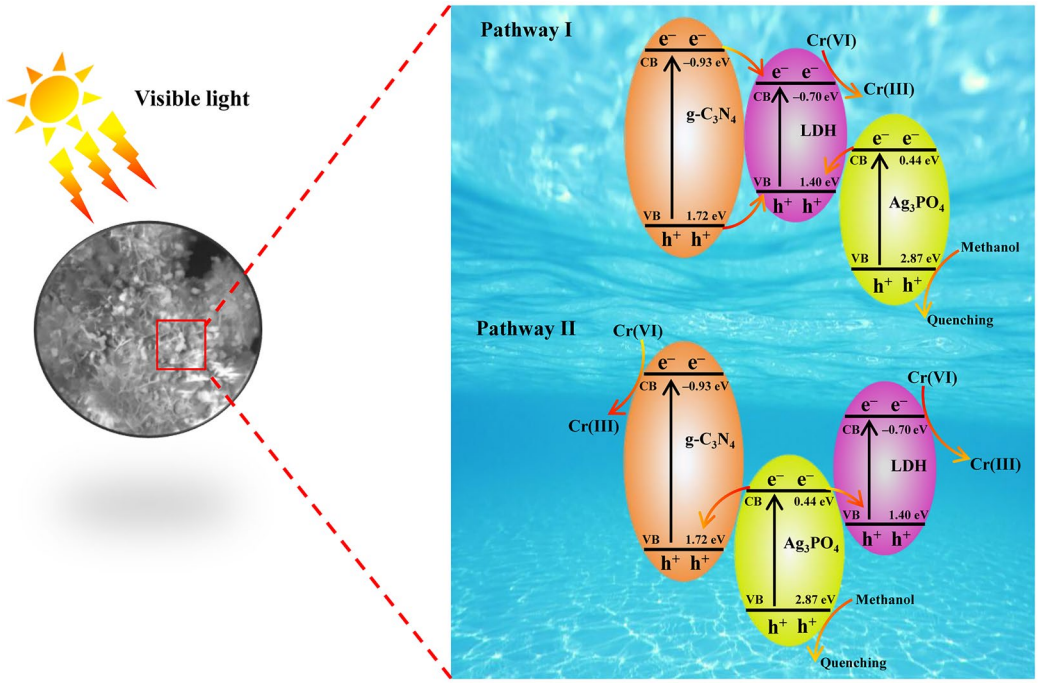

Fig. 9 Possible photocatalytic mechanism for the enhanced photocatalytic activity of the CNLDHAP composite photocatalyst

CONCLUSIONS

A multiple heterojunction system was constructed successfully using a two-step hydrothermal route. The photocatalytic activity of the CNLDHAP composite photocatalyst improved by 43.0–75.9% compared to the individual components, and the Cr(VI) reduction efficiency depended to a significant extent on the Ag_3PO_4 content. The optimum CNLDHAP70 showed the greatest photocatalytic activity for Cr(VI) reduction (96.0%), and the k value was ~15.67 and 11.75 times greater than that of g-C_3N_4 and LDH, respectively. CNLDHAP70 exhibited significant recycling stability: the Cr(VI) reduction efficiency remained at a high level after five cycles. The present study has provided new insights into the construction of multiple-heterojunction photocatalysts with improved separation efficiency of photogenerated carriers.

ACKNOWLEDGMENTS

This work was supported by the Key Research and Development Program of Hunan Province (2018SK20110).

Funding

Funding sources are as stated in the Acknowledgments.

Declarations

Conflict of Interest

The authors declare that they have no conflict of interest.

REFERENCES

Abroshan, E., Farhadi, S., & Zabardasti, A. (2018). Novel magnetically separable $Ag_3PO_4/MnFe_2O_4$ nanocomposite and its high photocatalytic degradation performance for organic dyes under solar-light irradiation. *Solar Energy Materials and Solar Cells, 178*, 154–163.

Chen, C., Zeng, H., Xu, S., Liu, X., Duan, H., & Han, J. (2017). Preparation of mesoporous material from hydrotalcite/carbon composite precursor for chromium(VI) removal. *Journal of the Taiwan Institute of Chemical Engineers, 70*, 302–310.

Chen, C. R., Zeng, H. Y., Xu, S., Shen, J. C., Hu, G., Zhu, R. L., Du, J. Z., & Sun, Y. X. (2018). Facile fabrication of CdS/ZnAlO heterojunction with enhanced photocatalytic activity for Cr(VI) reduction under visible light. *Applied Clay Science, 165*, 197–204.

Chen, C., Zeng, H., Yi, M., Xiao, G., Xu, S., Shen, S., & Feng, B. (2019a). In-situ growth of Ag_3PO_4 on calcined Zn-Al layered double hydroxides for enhanced photocatalytic degradation of tetracycline under simulated solar light irradiation and toxicity assessment. *Applied Catalysis B: Environmental, 252*, 47–54.

Chen, C., Zeng, H., Yi, M., Xiao, G., Zhu, R., Cao, X., Shen, S., & Peng, J. (2019b). Fabrication of Ag_2O/Ag decorated ZnAl-layered double hydroxide with enhanced visible light photocatalytic activity for tetracycline degradation. *Ecotoxicology and Environmental Safety, 172*, 423–431.

Das, S., Patnaik, S., & Parida, K. M. (2019). Fabrication of a Au-loaded $CaFe_2O_4$/CoAl LDH p–n junction based architecture with stoichiometric H_2 & O_2 generation and Cr(vi) reduction under visible light. *Inorganic Chemistry Frontiers, 6*, 94–109.

https://doi.org/10.1007/s42860-021-00121-0 Published online by Cambridge University Press

Dhanabal, R., Velmathi, S., & Chandra, A. (2018). Bose Fabrication of RuO_2-Ag_3PO_4 heterostructure nanocomposites: Investigations of band alignment on the enhanced visible light photocatalytic activity. *Journal of Hazardous Materials, 344*, 865–874.

Fang, J., Li, M., Li, Q., Zhang, W., Shou, Q., Liu, F., Zhang, X., & Cheng, J. (2012). Microwave-assisted synthesis of CoAl-layered double hydroxide/graphene oxide composite and its application in supercapacitors. *Electrochimica Acta, 85*, 248–255.

Fettkenhauer, C., Clavel, G., Kailasam, K., Antonietti, M., & Dontsova, D. (2015). Facile synthesis of new, highly efficient SnO_2/carbon nitride composite photocatalysts for the hydrogen evolution reaction. *Green Chemistry, 17*, 3350–3361.

Hu, J., Chen, D., Mo, Z., Li, N., Xu, Q., Li, H., He, J., Xu, H., & Lu, J. (2019). Z-Scheme 2D/2D Heterojunction of black phosphorus/monolayer Bi_2WO_6 nanosheets with enhanced photocatalytic activities. *Angewandte Chemie, 131*, 2095–2099.

Jing, F., Liang, R., Xiong, J., Chen, R., Zhang, S., Li, Y., & Wu, L. (2017). MIL-68(Fe) as an efficient visible-light-driven photocatalyst for the treatment of a simulated waste-water contain Cr(VI) and Malachite Green. *Applied Catalysis B: Environmental, 206*, 9–15.

Jo, W. K., & Tonda, S. (2019). Novel CoAl-LDH/g-C_3N_4/RGO ternary heterojunction with notable 2D/2D/2D configuration for highly efficient visible-light-induced photocatalytic elimination of dye and antibiotic pollutants. *Journal of Hazardous Materials, 368*, 778–787.

Kang, Q., Cao, J., Zhang, Y., Liu, L., Xu, H., & Ye, J. (2013). Reduced TiO_2 nanotube arrays for photoelectrochemical water splitting. *Journal of Materials Chemistry A, 1*, 5766–5774.

Kumar, S., Surendar, T., Baruah, A., & Shanker, V. (2013). Synthesis of a novel and stable g-C_3N_4–Ag_3PO_4 hybrid nanocomposite photocatalyst and study of the photocatalytic activity under visible light irradiation. *Journal of Materials Chemistry A, 1*, 5333–5340.

Kumar, S., Isaacs, M. A., Trofimovaite, R., Durndell, L., Parlett, C. M. A., Douthwaite, R. E., Coulson, B., Cockett, M. C. R., Wilson, K., & Lee, A. F. (2017). P25@CoAl layered double hydroxide heterojunction nanocomposites for CO_2 photocatalytic reduction. *Applied Catalysis B: Environmental, 209*, 394–404.

Li, H., Li, J., Xu, C., Yang, P., Ng, D. H. L., Song, P., & Zuo, M. (2017). Hierarchically porous MoS_2/CoAl-LDH/HCF with synergistic adsorption-photocatalytic performance under visible light irradiation. *Journal of Alloys and Compounds, 698*, 852–862.

Li, K., Huang, Z., Zhu, S., Luo, S., Yan, L., Dai, Y., Guo, Y., & Yang, Y. (2019). Removal of Cr(VI) from water by a biochar-coupled g-C_3N_4 nanosheets composite and performance of a recycled photocatalyst in single and combined pollution systems. *Applied Catalysis B: Environmental, 243*, 386–396.

Liu, Y., Zhu, G., Gao, J., Hojamberdiev, M., Zhu, R., Wei, X., Guo, Q., & Liu, P. (2017). Enhanced photocatalytic activity of $Bi_4Ti_3O_{12}$ nanosheets by Fe^{3+}-doping and the addition of Au nanoparticles: photodegradation of phenol and bisphenol A. *Applied Catalysis B: Environmental, 200*, 72–82.

Liu, X., Xu, J., Ni, Z., Wang, R., You, J., & Guo, R. (2019a). Adsorption and visible-light-driven photocatalytic properties of Ag_3PO_4/WO_3 composites: a discussion of the mechanism. *Chemical Engineering Journal, 356*, 22–33.

Liu, D., Chen, D., Li, N., Xu, Q., Li, H., He, J., & Lu, J. (2019). ZIF-67-Derived 3D Hollow Mesoporous crystalline Co_3O_4 wrapped by 2D g-C_3N_4 nanosheets for photocatalytic removal of nitric oxide. *Small, 15,* 1902291.

Luo, J., Luo, X., Crittenden, J., Qu, J., Bai, Y., Peng, Y., & Li, J. (2015). Removal of antimonite (Sb(III)) and antimonate (Sb(V)) from aqueous solution using carbon nanofibers that are decorated with zirconium oxide (ZrO_2). *Environmental Science & Technology, 49*, 11115–11124.

Luo, J., Sun, M., Ritt, C. L., Liu, X., Pei, Y., Crittenden, J. C., & Elimelech, M. (2019). Tuning Pb(II) adsorption from aqueous solutions on ultrathin iron oxychloride (FeOCl) nanosheets. *Environmental Science & Technology, 53*, 2075–2085.

Ma, R., Liang, J., Takada, K., & Sasaki, T. (2010). Topochemical synthesis of Co-Fe layered double hydroxides at varied Fe/Co ratios: unique intercalation of triiodide and its profound effect. *Journal of the American Chemical Society, 133*, 613–620.

Nanda, B., Pradhan, A. C., & Parida, K. M. (2017). Fabrication of mesoporous CuO/ZrO_2-MCM-41 nanocomposites for photocatalytic reduction of Cr(VI). *Chemical Engineering Journal, 316*, 1122–1135.

Peng, W., Li, H., & Song, S. (2017a). Synthesis of fluorinated graphene/CoAl-layered double hydroxide composites as electrode materials for supercapacitors. *ACS Applied Materials & Interfaces, 9*, 5204–5212.

Peng, W., Li, H., Liu, Y., & Song, S. (2017b). Effect of oxidation degree of graphene oxide on the electrochemical performance of CoAl-layered double hydroxide/graphene composites. *Applied Materials Today, 7*, 201–211.

Shakeel, M., Arif, M., Yasin, G., Li, B., & Khan, H. D. (2019). Layered by layered Ni-Mn-LDH/g-C_3N_4 nanohybrid for multi-purpose photo/electrocatalysis: Morphology controlled strategy for effective charge carriers separation. *Applied Catalysis B: Environmental, 242*, 485–498.

Shao, B., Liu, X., Liu, Z., Zeng, G., Liang, Q., Liang, C., Cheng, Y., Zhang, W., Liu, Y., & Gong, S. (2019). A novel double Z-scheme photocatalyst Ag_3PO_4/Bi_2S_3/Bi_2O_3 with enhanced visible-light photocatalytic performance for antibiotic degradation. *Chemical Engineering Journal, 368*, 730–745.

Sun, Q., Hu, X., Zheng, S., Zhang, J., & Sheng, J. (2019). Effect of calcination on structure and photocatalytic property of N-TiO_2/g-C_3N_4@diatomite hybrid photocatalyst for improving reduction of Cr(VI). *Environmental Pollution, 245*, 53–62.

Tan, P., Chen, X., Wu, L., Shang, Y., Liu, W., Pan, J., & Xiong, X. (2017). Hierarchical flower-like $SnSe_2$ supported Ag_3PO_4 nanoparticles: towards visible light driven photocatalyst with enhanced performance. *Applied Catalysis B: Environmental, 202*, 326–334.

Tian, L., Yang, X., Cui, X., Liu, Q., & Tang, H. (2019). Fabrication of dual direct Z-scheme g-C_3N_4/MoS_2/Ag_3PO_4 photocatalyst and its oxygen evolution performance. *Applied Surface Science, 463*, 9–17.

Tonda, S., Kumar, S., Bhardwaj, M., Yadav, P., & Ogale, S. (2018). g-C_3N_4/NiAl-LDH 2D/2D hybrid heterojunction for high-performance photocatalytic reduction of CO_2 into renewable fuels. *ACS Applied Materials & Interfaces, 10*, 2667–2678.

Velegraki, G., Miao, J., Drivas, C., Liu, B., Kennou, S., & Armatas, G. S. (2018). Fabrication of 3D mesoporous networks of assembled CoO nanoparticles for efficient photocatalytic reduction of aqueous Cr(VI). *Applied Catalysis B: Environmental, 221*, 635–644.

Wan, J., Du, X., Liu, E., Hu, Y., Fan, J., & Hu, X. (2017). Z-scheme visible-light-driven Ag_3PO_4 nanoparticle@MoS_2 quantum dot/few-layered MoS_2 nanosheet heterostructures with high efficiency and stability for photocatalytic selective oxidation. *Journal of Catalysis, 345*, 281–294.

Wang, S., Li, C., Wang, T., Zhang, P., Lia, A., & Gong, J. (2014). Controllable synthesis of nanotube-type graphitic C_3N_4 and their visible-light photocatalytic and fluorescent properties. *Journal of Materials Chemistry A, 2*, 2885–2890.

Wang, K., Zhang, L., Su, Y., Shao, D., Zeng, S., & Wang, W. (2018). Photoreduction of carbon dioxide of atmospheric concentration to methane with water over CoAl-layered double hydroxide nanosheets. *Journal of Materials Chemistry A, 6*, 8366–8373.

Wang, X., Liu, W., Fu, H., Yi, X., Wang, P., Zhao, C., Wang, C., & Zheng, W. (2019). Simultaneous Cr(VI) reduction and Cr(III) removal of bifunctional MOF/Titanate nanotube composites. *Environmental Pollution, 249*, 502–511.

Wu, J., Wang, J., Du, Y., Li, H., Yang, Y., & Jia, X. (2015). Chemically controlled growth of porous CeO_2 nanotubes for Cr(VI) photoreduction. *Applied Catalysis B: Environmental, 174*, 435–444.

Wu, Y., Wang, H., Sun, Y., Xiao, T., Tu, W., Yuan, X., Zeng, G., Li, S., & Chew, J. W. (2018). Photogenerated charge transfer via interfacial internal electric field for significantly improved photocatalysis in direct Z-scheme oxygen-doped carbon nitrogen/CoAl-layered double hydroxide heterojunction. *Applied Catalysis B: Environmental, 227*, 530–540.

Xu, H., Wang, C., Song, Y., Zhu, J., Xu, Y., Yan, J., Song, Y., & Li, H. (2014). CNT/Ag_3PO_4 composites with highly enhanced visible light photocatalytic activity and stability. *Chemical Engineering Journal, 241*, 35–42.

Xu, T., Zhu, R., Zhu, G., Zhu, J., Liang, X., Zhu, Y., & He, H. (2017). Mechanisms for the enhanced photo-Fenton activity of ferrihydrite modified with $BiVO_4$ at neutral pH. *Applied Catalysis B: Environmental, 212*, 50–58.

Yang, W., Li, J., Liu, M., Ng, D. H. L., Liu, Y., Sun, X., & Yang, J. (2019). Bioinspired hierarchical CoAl-LDH/MFe_2O_4 (Ni, Zn, Co) as peroxidase mimics for colorimetric detection of glucose. *Applied Clay Science, 181*, 105238–105249.

Yuan, R., Yue, C., Qiu, J., Liu, F., & Li, A. (2019). Highly efficient sunlight-driven reduction of Cr(VI) by TiO_2@NH_2-MIL-88B(Fe) heterostructures under neutral conditions. *Applied Catalysis B: Environmental, 251*, 229–239.

Zhang, L., Li, L., Sun, X., Liu, P., Yang, D., & Zhao, X. (2016a). ZnO-layered double hydroxide@graphitic carbon nitride composite for consecutive adsorption and photodegradation of dyes under UV and visible lights. *Materials, 9*, 927.

Zhang, S., Zhang, Y., Jiang, W., Liu, X., Xu, S., Huo, R., Zhang, F., & Hu, J. (2016b). Co@N-CNTs derived from triple-role CoAl-layered double hydroxide as an efficient catalyst for oxygen reduction reaction. *Carbon, 107*, 162–170.

Zhao, Y., Chen, G., Bian, T., Zhou, C., Waterhouse, G. I. N., Wu, L., Tung, C. H., Smith, L. J., O'Hare, D., & Zhang, T. (2015). Defect-rich ultrathin ZnAl-layered double hydroxide nanosheets for efficient photoreduction of CO_2 to CO with water. *Advanced Materials, 27*, 7824–7831.

Zhao, Y., Jia, X., Waterhouse, G. I. N., Wu, L., Tung, C. H., O'Hare, D., & Zhang, T. (2016). Layered double hydroxide nanostructured photocatalysts for renewable energy production. *Advanced Energy Materials, 6*, 1501974.

Zheng, Y., Lin, L., Wang, B., & Wang, X. (2015). Graphitic carbon nitride polymers toward sustainable photoredox catalysis. *Angewandte Chemie International Edition, 54*, 12868–12884.

Zhong, Y., Qiu, X., Chen, D., Li, N., Xu, Q., Li, H., He, J., & Lu, J. (2016). Flexible electrospun carbon nanofiber/tin(IV) sulfide core/sheath membranes for photocatalytically treating chromium(VI)-containing wastewater. *ACS Applied Materials & Interfaces, 8*, 28671–28677.

Zhou, L., Zhang, W., Chen, L., & Deng, H. (2017). Z-scheme mechanism of photogenerated carriers for hybrid photocatalyst Ag_3PO_4/g-C_3N_4 in degradation of sulfamethoxazole. *Journal of Colloid and Interface Science, 487*, 410–417.

(Received 16 September 2020; revised 8 March 2021; AE: Jun Kawamata)